Key Points:
- Basal melting at a single location beneath the outer Pine Island Ice Shelf is highly variable on weekly to monthly timescales throughout 2014
- Adjustment of the upper thermocline to local wind forcing is the dominant control on this short timescale variability
- When longer timescale processes drive a deeper thermocline in Pine Island Bay, wind-forced high-frequency variability in the basal melt rate appears to be suppressed

Correspondence to:
P. E. D. Davis,
petvis@bas.ac.uk

Variability in Basal Melting Beneath Pine Island Ice Shelf on Weekly to Monthly Timescales

Peter E. D. Davis[1] (iD), **Adrian Jenkins[1]** (iD), **Keith W. Nicholls[1]** (iD), **Paul V. Brennan[2]**, **E. Povl Abrahamsen[1]**, **Karen J. Heywood[3]** (iD), **Pierre Dutrieux[4]** (iD), **Kyoung-Ho Cho[5]** (iD), and **Tae-Wan Kim[5]** (iD)

[1]British Antarctic Survey, Natural Environment Research Council, Cambridge, UK, [2]Department of Electronic and Electrical Engineering, University College London, London, UK, [3]Centre for Ocean and Atmospheric Sciences, University of East Anglia, Norwich, UK, [4]Lamont-Doherty Earth Observatory, Columbia University, Palisades, NY, USA, [5]Korea Polar Research Institute, Incheon, South Korea

Abstract Ocean-driven basal melting of Amundsen Sea ice shelves has triggered acceleration, thinning, and grounding line retreat on many West Antarctic outlet glaciers. Here we present the first year-long (2014) record of basal melt rate at sub-weekly resolution from a location on the outer Pine Island Ice Shelf. Adjustment of the upper thermocline to local wind forced variability in the vertical Ekman velocity is the dominant control on basal melting at weekly to monthly timescales. Atmosphere-ice-ocean surface heat fluxes or changes in advection of modified Circumpolar Deep Water play no discernible role at these timescales. We propose that during other years, a deepening of the thermocline in Pine Island Bay driven by longer timescale processes may have suppressed the impact of local wind forcing on high-frequency upper thermocline height variability and basal melting. This highlights the complex interplay between the different processes and their timescales that set the basal melt rate beneath Pine Island Ice Shelf.

Plain Language Summary Ice shelves—the floating extensions of the Antarctic ice sheet—are melted from beneath when in contact with warm ocean waters. The rate at which they melt is especially important for controlling Antarctica's contribution to future sea level rise, and extreme basal melting may even be capable of causing the West Antarctic Ice Sheet to rapidly collapse. Here we use the first high resolution time series of basal melting observed beneath Pine Island Ice Shelf in the Amundsen Sea sector of West Antarctica to explore what sets the melt rate on short timescales. We find that during 2014, the local wind patterns are particularly important, as they are capable of changing the ocean temperature beneath Pine Island Ice Shelf. In other years, however, local wind patterns seem less important, highlighting the complex interactions that exist between the ice shelf and the ocean upon which it floats.

1. Introduction

Ice shelves in the Amundsen Sea sector of West Antarctica (Figure 1) are thinning (Paolo et al., 2015; Pritchard et al., 2012; Shepherd et al., 2018). The geographic coherence of the thinning signal (Paolo et al., 2015) implicates changes in ocean forcing as the likely cause. Because these ice shelves buttress the fast-flowing outlet glaciers that drain the West Antarctic Ice Sheet (Fürst et al., 2016), ocean-driven basal melting has triggered acceleration (Mouginot et al., 2014), thinning (McMillan et al., 2014), and mass loss (IMBIE, 2018) from grounded ice upstream, as well as grounding line retreat (Rignot et al., 2014; Scheuchl et al., 2016). This has major implications for marine ice sheet stability (Bamber et al., 2009) and global sea level rise (Shepherd et al., 2012), with some models suggesting Antarctica could contribute >1 m to global mean sea level by 2100 (DeConto & Pollard, 2016). It is, therefore, critically important that we understand the dynamic links and their timescales between basal melting and ocean conditions in the Amundsen Sea.

Pine Island Glacier (PIG) is one of the largest and fastest flowing outlet glaciers in the Amundsen Sea sector. It has exhibited near continuous thinning (Wingham et al., 2009) and intermittent acceleration (Mouginot et al., 2014) over the observational era, and it terminates in the rapidly melting Pine Island Ice Shelf (PIIS; Figure 1). Basal melting beneath PIIS is driven by modified warm Circumpolar Deep Water (mCDW) that is forced onto the Amundsen Sea continental shelf through troughs in the shelf break (Wåhlin et al., 2010; Walker et al., 2013). Separated from the cold and fresh surface Winter Water (WW) layer by a thermocline between 300 and 700 m, the mCDW is guided southward toward Pine Island Bay (PIB) and into the sub-ice shelf cavity through a network of glacially carved troughs (Jacobs et al., 2011; Mallett et al., 2018). Here the mCDW
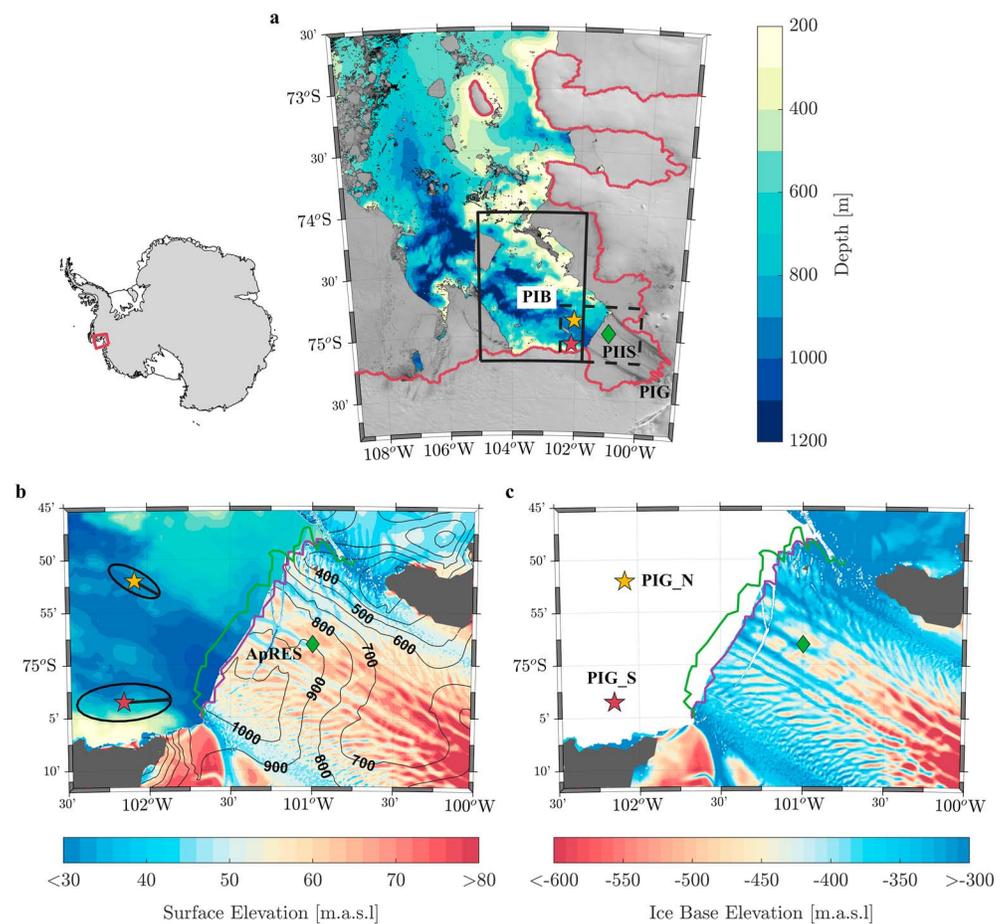
Figure 1. Location and geometry of Pine Island Glacier. (a) Moderate Resolution Imaging Spectroradiometer (MODIS) image from January 2014 of Pine Island Bay with International Bathymetric Chart of the Southern Ocean bathymetry (Arndt et al., 2013) and grounding line position (Bindschadler et al., 2011). Pine Island Ice Shelf (PIIS), Pine Island Glacier (PIG), and Pine Island Bay (PIB) are labeled. The solid black box marks the area over which the atmosphere-ice-ocean surface heat flux and vertical Ekman velocity are averaged. (b) PIIS 2014 surface and (c) ice base elevation from the area indicated by the black dashed box in (a) from a high resolution digital elevation model (Shean, 2016; Shean et al., 2016). Purple and green lines mark the ice front location in January and December 2014, respectively. The black contours in (b) show the sub-ice shelf bathymetry (Millan et al., 2017). The location of the autonomous phase-sensitive radio-echo sounder is marked by the green diamond, the southern ocean mooring (PIG_S) by the red star, and the northern ocean mooring (PIG_N) by the yellow star. The black ellipses and arrows in (b) show the horizontal velocity variance ellipses and the direction of PIG-wards currents at the northern and southern moorings.

layer must pass over a 700-m deep topographic ridge before ultimately reaching the grounding line (Jenkins et al., 2010). The thickness of the mCDW layer that passes over this ridge controls the supply of heat to the grounding line; thus, variability in the depth of the thermocline exerts a strong control on basal melting (De Rydt et al., 2014; Dutrieux, De Rydt, et al., 2014). This variability is now understood to be critically important for ice shelf-ocean interactions in the Amundsen Sea sector (Jenkins et al., 2016). Indeed, when strong variability is superimposed upon a weak background trend, extrema in ocean conditions can trigger step changes in the behaviour of an ice shelf, which cannot be readily reversed by a change in the sign of the background trend.

Thermocline height in PIB and the wider Amundsen Sea varies seasonally and interannually. On seasonal timescales, the mCDW layer upstream of PIB in the northeastern Amundsen Sea is deeper, saltier, and warmer in winter than in summer (Mallett et al., 2018). Closer to PIIS, seasonal changes are less coherent, and hydrographic data collected through seal tagging suggest that conditions are highly variable in space (Mallett et al., 2018). Part of this variability is likely related to the cyclonic gyre that exists in PIB (Heywood

et al., 2016; Thurnherr et al., 2014), and the combined impact that its mixing, recirculation, and seasonal spin-up and spin-down has on the vertical position of isopycnals and water mass distribution.

On longer timescales, the thermocline in PIB shoaled between 1994 and 2009 by more than 100 dbar and warmed by 0.45 °C between 200 and 700 dbar (Jacobs et al., 2011). The shoaling allowed more mCDW to flow over the sub-ice shelf ridge, leading to a 50% increase in meltwater production. In contrast, a deepening of the thermocline between January 2010 and 2012 resulted in a 50% reduction in oceanic melting as deduced from hydrographic observations (Dutrieux, De Rydt, et al., 2014) and was the start of a long term cooling trend that by the beginning of 2013 had resulted in a 62% reduction in heat content in front of PIIS (Christianson et al., 2016; Webber et al., 2017). The deepening of the thermocline and the corresponding reduction in heat content has been ascribed to variability in local atmospheric surface forcing, sea ice formation, and ocean circulation in PIB (Webber et al., 2017), as well as an increase in the strength of easterly winds at the shelf edge suppressing the on-shelf transport of mCDW (Thoma et al., 2008). While models suggest that variability in shelf edge winds is important for setting the basal melt rate beneath many of the Amundsen Sea ice shelves on interannual timescales (Deb et al., 2018; Kimura et al., 2017), it remains somewhat unclear whether these shelf edge winds, or local atmospheric forcing in PIB itself, are the main driver for setting thermocline height in PIB on interannual timescales.

Although observations suggests that basal melting was greatly reduced over the same period (2010 to 2013; Dutrieux, De Rydt, et al., 2014), only a small reduction in the flow speed of PIG and its ice shelf was observed (Christianson et al., 2016; Shean et al., 2017). The limited reduction in flow speed (<4%) compared with the change in melt rate highlights the complex relationship that exists between the ocean forcing that sets the melt rate and the dynamic response of the ice shelf-glacier system that also depends on the geometry of the ice shelf and its cavity (Jenkins et al., 2016).

Thermocline depth has also been implicated as the driver of melt rate variability for a number of other ice shelves. A significant decrease in melting beneath Wilkins Ice Shelf (WIS) on the western side of the Antarctic Peninsula was observed in 2000 (Padman et al., 2012). The base of WIS sits within the thermocline that separates the warm mCDW from the cold WW, and it was concluded that a small increase in the depth of this interface drove the reduction in basal melting (Padman et al., 2012). Similarly, interannual variability in the velocity of Totten Ice Shelf, East Antarctica, is sensitive to changes in wind-forced upwelling that shoals the thermocline and increases the volume of mCDW on the continental shelf (Greene et al., 2017), although polynya dynamics may also be important (Khazendar et al., 2013). A comparable process has also been observed in the Amundsen Sea Dotson Trough, with seasonal changes in the vertical Ekman velocity increasing the thickness of the mCDW layer that flows southward toward the Dotson and Getz ice shelves (Kim et al., 2017).

These studies have built a coherent picture of how local and remote forcing of thermocline depth in the vicinity of Antarctic ice shelves can drive seasonal to interannual variability in their basal melt rate. Here we explore whether changes in thermocline depth are also responsible for setting the basal melt rate on shorter, sub-seasonal, timescales. We compare a novel, year-long (2014) time series of basal melt rate beneath PIIS (Lok et al., 2018) with observations from two oceanographic moorings deployed close to the ice shelf front and atmospheric reanalysis data averaged over PIB (Figure 1). The sub-weekly resolution of the melt rate time series observed using an autonomous phase-sensitive radio echo-sounder (ApRES) allows us, for the first time, to explore the high-frequency response of PIIS to changes in ocean and atmospheric conditions in PIB. By exploring timescales of variability that have never been studied before, this work significantly improves our understanding of how sub-seasonal atmosphere-ocean forcing interacts with Pine Island Glacier and its ice shelf.

2. Data and Methods

2.1. Autonomous Phase-Sensitive Radio Echo-Sounder (ApRES)

The ApRES was deployed on the outer PIIS in January 2014 at a location approximately 10 km from the ice shelf front where the ice was 492-m thick (ice shelf draft approximately 422 m; 74°58.38′S, 100°59.52′W; Figure 1). Following the method developed by Nicholls et al. (2015), the raw Lagrangian ice shelf thinning rate at two-hourly resolution was derived from the time derivative of the distance between the ApRES antennas and the ice shelf base and includes the basal melt rate signal as well as a component of ice-column vertical strain rate resulting from ice flow and snow compaction. To remove the component of ice-column vertical

strain rate due to tidal variations, the raw thinning rate was low-pass filtered using a cutoff at 48 hr. At frequencies lower than this, variability in the strain rate component is small compared with the melt rate and varies on a much longer timescale than those of interest here. Overall, the ApRES returned a 323-day time series of ice shelf basal melt rate with an accuracy of ±0.2 m/year.

2.2. Ocean Moorings

In addition to the ApRES, two oceanographic moorings were deployed in PIB between 16 and 18 February 2014 and 2 February 2016, contributing to the continuous time series of ocean measurements in PIB that dates back to 2009 (Heywood et al., 2016; Webber et al., 2017). The southern mooring (75°03.53′S, 102°09.14′W) was deployed within 10 km of the main meltwater outflow from PIIS in 732 m of water, while the northern mooring was deployed in the center of PIB in 956 m of water (74°51.79′S, 102°06.25′W; Figure 1). The moorings were instrumented at discrete depths below 445 m at the northern mooring, and 320 m at the southern mooring (the nominal interval between instruments was 50 to 80 m), and measured temperature, salinity, pressure, and ocean velocity at time intervals ranging from 5 to 30 min (Webber et al., 2017).

Heat content above the surface-referenced freezing point over the depth range z_1 to z_2 is calculated from

$$H = \int_{z1}^{z2} \rho_\Theta c_p (\Theta - \Theta_f) \, dz,$$

where ρ_Θ is the potential density, c_p the ocean heat capacity, Θ the conservative temperature interpolated onto a 1-m depth grid, and Θ_f the surface-referenced freezing point calculated using the TEOS-10 equation of state (McDougall & Barker, 2011). Since the freezing point depends upon salinity, which was not observed by the majority of the mooring instruments, the method of Webber et al. (2017) was used to infer salinity directly from temperature. Assuming an uncertainty in salinity of ±0.3 g/kg, the uncertainty in the freezing point is ±0.02 °C.

The direction of PIG-wards flow at each mooring location is defined as the angle between geographic north and the maximum in the horizontal velocity variance ellipse in the direction of PIIS (Figure 1b; Webber et al., 2017). For the southern and northern mooring, respectively, this direction is 87° and 129°. Small changes in the angle of PIG-wards flow do not affect the results of this study.

2.3. Atmospheric Reanalysis Products

To complement the observations, the surface heat flux averaged over PIB (74.0°–75.2°S, 105.0°–101.8°W; Figure 1) was derived from the latest European Centre for Medium-Range Weather Forecasts (ECMWF) climate reanalysis product, ERA5 (ECMWF, 2018a), the Climate Forecast System Reanalysis (CFSR; Saha et al., 2010), and from the method described by Tamura et al. (2008, 2011). A comparison with the limited observations in the region has shown that ERA-Interim (the precursor to ERA5; Dee et al., 2011), and CFSR are the best performing reanalysis products over the Amundsen Sea, and ERA5 is known to perform better than ERA-Interim in the troposphere (ECMWF, 2018b). Nevertheless, the reanalysis products still contain large uncertainties and biases due to, for example, sparse observational constraints and the coarse resolution in near-coastal regions (Jones et al., 2016).

The surface heat flux is defined as

$$Q_{net} = Q_{SW}(1 - \alpha) + Q_{LW} + Q_L + Q_S,$$

where Q_{SW} is the incoming shortwave radiation, α the albedo, Q_{LW} the outgoing longwave radiation, Q_L the latent heat flux, and Q_S the sensible heat flux. Positive values of Q_{net} indicate heat input to the ocean. The land mask from each reanalysis products is used to blank values over land.

In addition, the vertical Ekman velocity derived from ERA5 and CFSR is calculated from the surface wind stress curl as

$$w_{ek} = \frac{1}{\rho f_\Omega} \left(\frac{\partial \tau_y}{\partial x} - \frac{\partial \tau_x}{\partial y} \right),$$

where ρ is density, f_Ω the Coriolis parameter, τ_y the meridional atmosphere-ocean wind stress, and τ_x the zonal atmosphere-ocean wind stress. Derivatives are calculated using first differences. The land mask from
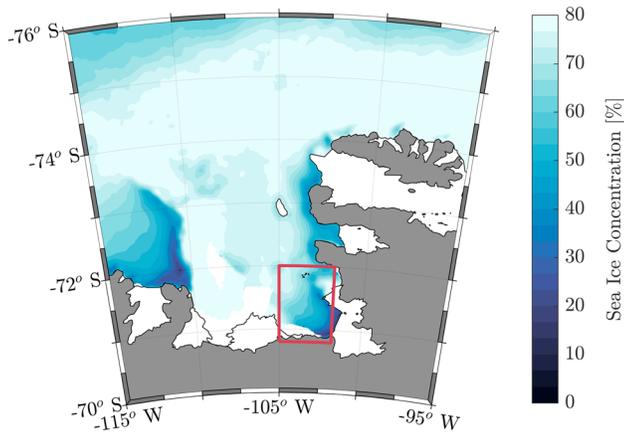
Figure 2. The 2014 mean sea ice concentration over the Amundsen Sea and Pine Island Bay from the Advanced Scanning Microwave Radiometer 2 (AMSR2; Spreen et al., 2008). The red box marks the area over which the vertical Ekman velocity is averaged.

each reanalysis product is used to blank values over land, meaning that w_{ek} is not computed for grid cells next to the coast. Therefore, in this study we are not considering the role of coastal upwelling and downwelling, a choice that is justified by the relatively poor representation of the coastline in the different reanalyses. In ice covered waters, the atmosphere-ocean wind stress is modified by the presence of sea ice. In this case the total ocean surface stress is given by a combination of the atmosphere-ocean wind stress over open water and the ice-ocean stress over sea ice (Kim et al., 2017). Calculating the ice-ocean stress, however, requires an estimate of the ice drift velocity, which has a native resolution of 25 km (Tschudi et al., 2016) and is not available in the area of PIB where we calculate the vertical Ekman velocity. Therefore, here we only consider the contribution of the atmosphere-ocean wind stress curl to the vertical Ekman velocity. Given the presence of the polynya in PIB that reduces the sea ice concentration (Figure 2) and the strong correlation that we observe in this paper between the melt rate and the vertical Ekman velocity calculated from wind stress curl alone, we believe that the missing ice-ocean stress does not play a leading order role here.

2.4. Magnitude-Squared Coherence

The magnitude-squared coherence estimates the degree of linear correlation between two time series x and y as a function of frequency. It is calculated as

$$C_{xy}(f) = \frac{\left|P_{xy}(f)\right|^2}{P_{xx}(f)P_{yy}(f)},$$

where $P_{xy}(f)$ is the cross-spectral density of x and y at frequency f and $P_{xx}(f)$ and $P_{yy}(f)$ are the power spectral densities of x and y, respectively. The squared coherence at any frequency represents the fraction of variance in x ascribable to y at that frequency. The 95% significance level is estimated through a bootstrap method. One time series, y, is randomly reordered many times to create a group of synthetic time series that have no correlation with x. The coherence between x and all the synthetic reordered time series is then calculated. This provides a distribution of coherence for all frequencies of the uncorrelated series, from which the significance level is derived.

The frequency-dependent time lag between x and y is calculated from the phase of the cross spectrum, $P_{xy}(f)$, as

$$\phi(f) = \tan^{-1}\left(\frac{\Im P_{xy}(f)}{\Re P_{xy}(f)}\right),$$

where $\Im$ is the imaginary part, $\Re$ is the real part, and we use a four-quadrant inverse tangent.

All time series presented in this study (ApRES, oceanographic, and atmospheric reanalysis) have been treated identically, apart from the ApRES thinning rate which has been additionally low-pass filtered with a cut-off at 48 hr to remove the component of vertical strain rate due to tidal variations. Daily averaged time series are used in the calculation of the magnitude-squared coherence to ensure each of the different time series are on the same temporal basis.

3. Results

3.1. Basal Melt Rate and Thermocline Depth

Basal melting beneath PIIS at the location of the ApRES shows considerable variability around a mean melt rate of 3.1 m/year (95% confidence interval: 3.06 m/year to 3.18 m/year; Figure 3a). As the ApRES is located only 10 km from the ice shelf front (Figure 1), the mean melt rate is significantly lower than the highest melt rates observed nearer the grounding line (Dutrieux et al., 2013). With the caveat that the time series is only one year long, there is no indication of an annual cycle. Strong variability exists at monthly to weekly frequencies, with a prominent peak in the variance-preserving form of the melt rate power spectrum at a frequency
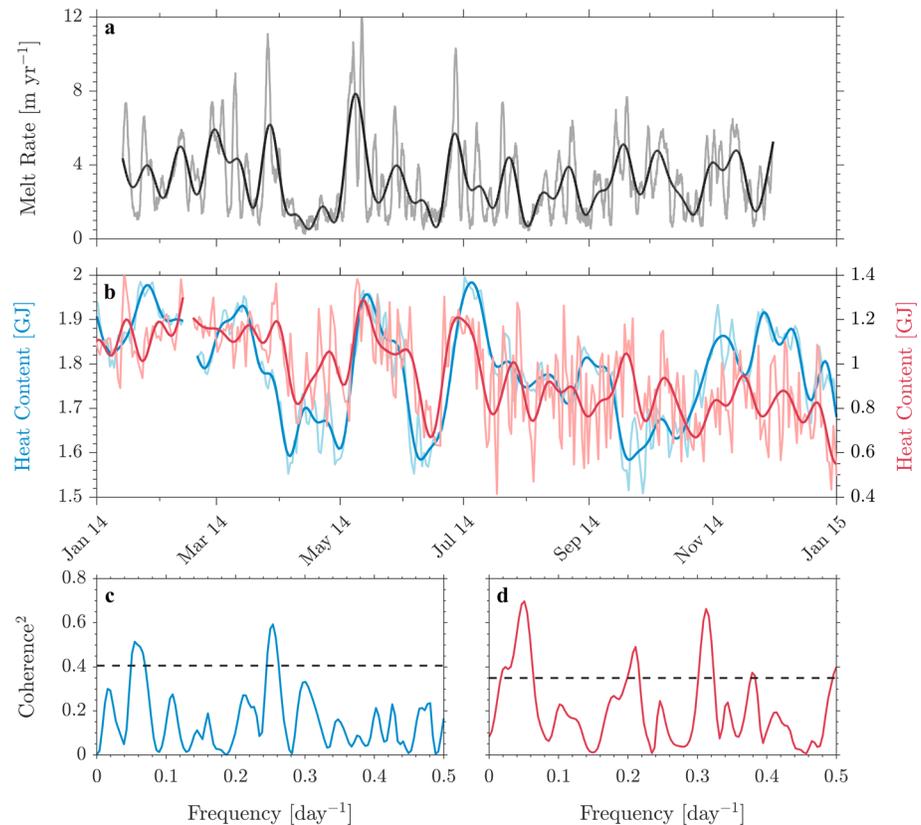
Figure 3. Melt rate beneath Pine Island Ice Shelf and integrated heat content in Pine Island Bay. (a) Time series of basal melt rate measured by the autonomous phase-sensitive radio-echo sounder and (b) ocean heat content integrated between 450 and 600 m at the northern ocean mooring (PIG_N; blue) and 325 and 475 m at the southern ocean mooing (PIG_S; red). The uncertainty in the heat content is approximately 1.5% of its mean value. Thick lines in (a) and (b) have been smoothed with a 10- to 15-day low-pass Kaiser-Bessel filter in order to isolate monthly and longer timescale variability. (c, d) Magnitude-squared coherence between the daily averaged basal melt rate and the daily averaged integrated ocean heat content at (c) the northern and (d) the southern ocean mooring. The black dashed line in (c) and (d) marks the 95% confidence level.

of 0.18 day^{-1} (Figure 4). At times (e.g., May 2014), the melt rate increases dramatically from close to 1 m/year to more than 10 m/year within 2 to 3 weeks, before decreasing at a similar rate.

Beneath the ApRES the ice shelf draft is approximately 422 m, and thus the base of the ice shelf sits within the upper mCDW thermocline (Dutrieux, De Rydt, et al., 2014; Jacobs et al., 2011; Figure 5c). Variability in the depth of the thermocline is characterized by calculating the integrated ocean heat content over the shallowest 150 m of the water column covered by each oceanographic mooring (Figures 3b and 5). A deeper thermocline is characterized by a reduced heat content, as the cold WW layer penetrates further into the water column and creates conditions that favor weaker melting. In contrast, a shallower thermocline leads to a thicker mCDW layer, higher heat content, and melting-favorable conditions. Variability in the ocean heat content is well correlated with the basal melt rate at both mooring locations, with the magnitude-squared coherence (Figures 3c and 3d) showing significant peaks at both monthly (0.05 day^{-1}) and weekly (0.2 to 0.3 day^{-1}) frequencies. We conclude that variability in thermocline depth is responsible for setting the basal melt rate on weekly to monthly timescales.

The correlation between heat content and melt rate is stronger for the southern mooring than for the northern mooring. We attribute this difference to the differing observational depths in comparison to the ice shelf draft at the location of the ApRES (422 m; black dashed line in Figure 5). While at the southern mooring the shallowest observational depth in 2014 was 320 m, 100 m shallower than the ice shelf draft, at the northern mooring the shallowest observational depth was 448 m, nearly 30 m deeper than the ice shelf draft (Figure 5). We postulate that at these greater depths, the processes that drive thermocline variability at sub-seasonal timescales are less readily felt, likely due to a reduction in the strength of the stratification and the attenuation of Ekman-
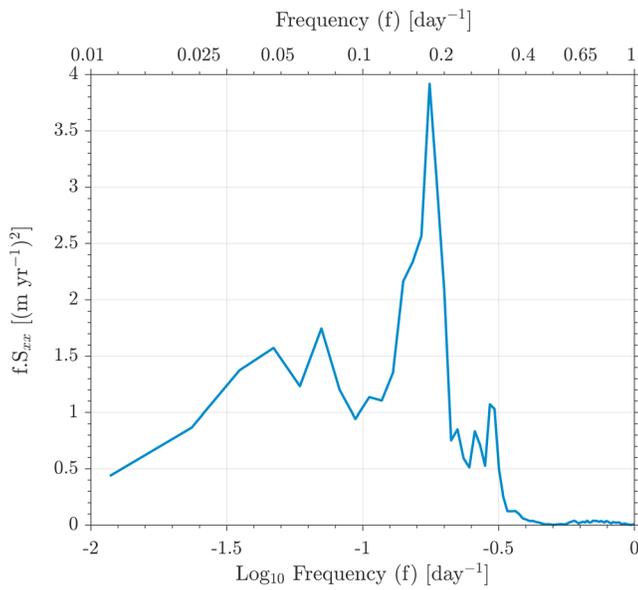
Figure 4. Variance-preserving form of the autonomous phase-sensitive radio-echo sounder melt rate power spectrum ($f. S_{xx}$), where the power spectrum (or power spectral density), S_{xx}, has been multiplied by frequency, f. In this variance preserving form, the area under the curve between two frequencies is equal to the contribution that temporal variability in that frequency band makes to the total signal variance (Emery & Thompson, 2001). The threshold of the low-pass filter with a cutoff at 48 hr that was used to remove variability at tidal timescales that might be contaminated by tidal variations in the strain rate is clearly visible at $\log_{10}(f) = -0.3$. The prominent peak at weekly timescales ($f = 0.18$ day^{-1}) is visible at $\log_{10}(f) = -0.75$.

driven heave with depth. As a result, the correlation between heat content and melt rate for the northern mooring is suppressed compared with that for the southern mooring. Logically, as the draft of PIIS increases with distance from the ice shelf front (Figures 1b and 1c), this suggests that a geographical limit will eventually be reached, beyond which the ice shelf base is too deep to be affected by high-frequency variability. Thus, the mechanisms discussed in this paper are most applicable to the outer PIIS (i.e., mostly seaward of the sub-ice shelf topographic ridge).

### 3.2. Drivers of Melt Rate Variability

At the weekly to monthly timescales being considered here, there are several major oceanic processes that can significantly alter the depth of the thermocline and thus the basal melt rate: atmosphere-ice-ocean surface heat fluxes that drive sea ice production and melt, dynamic forcing of the thermocline through Ekman pumping, and changes in advection of mCDW toward PIIS. Based on the available observations in this study, changes in advection of mCDW do not appear to be important for setting the basal melt rate at monthly timescales: the magnitude-squared coherence between melt rate and PIG-wards current velocity at a depth of 650 m at the northern oceanographic mooring (the shallowest velocity observation available) does not exceed 0.1 (not shown). While it is possible that advection of mCDW toward PIIS may be relatively more important at depths shallower than 650 m, we cannot assess its role further here.

ERA5- (ECMWF, 2018a), CFSR- (Saha et al., 2010), and Tamura- (Tamura et al., 2008, 2011) derived surface heat flux anomalies averaged over PIB (black box in Figure 1a) all show a clear annual cycle around mean values of -23.6 W/m^2, -82.5 W/m^2, and -41.6 W/m^2, respectively (Figure 6a). The discrepancies in the mean value are due to the errors that are inherent to all reanalysis products in this region (Jones et al., 2016). Despite this, anomalies in the different reanalysis products are well correlated, and the average magnitude-squared coherence between the surface heat flux anomalies and the basal melt rate is significant at monthly timescales (0.05 day^{-1}; Figure 6c).
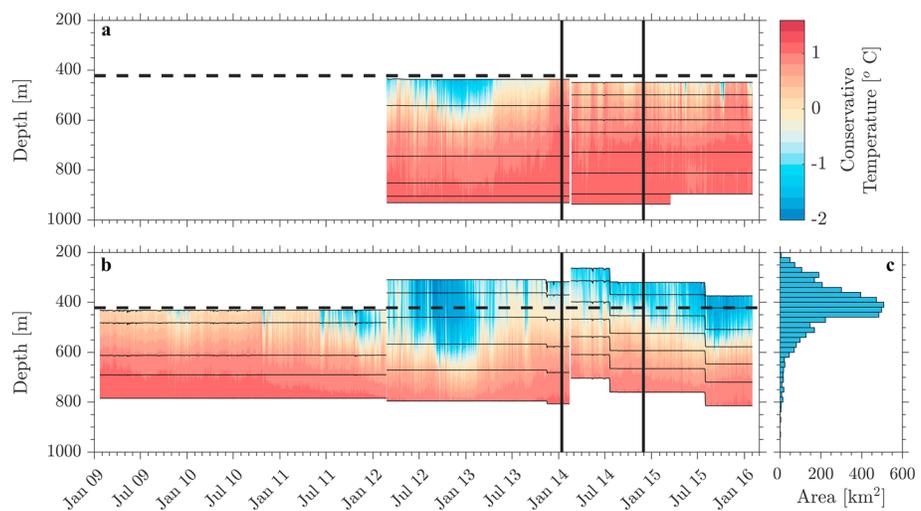

Figure 5. Ocean conditions in Pine Island Bay. Conservative temperature Hovmöller plots from (a) the northern mooring and (b) the southern mooring deployed in Pine Island Bay. The solid black lines indicate the observational period of the autonomous phase-sensitive radio-echo sounder (ApRES), while the black dashed line indicates the ice shelf draft at the location of the ApRES. The thin black lines indicate the depths of the different mooring instruments. (c) Histogram of Pine Island Ice Shelf draft from Bedmap2.
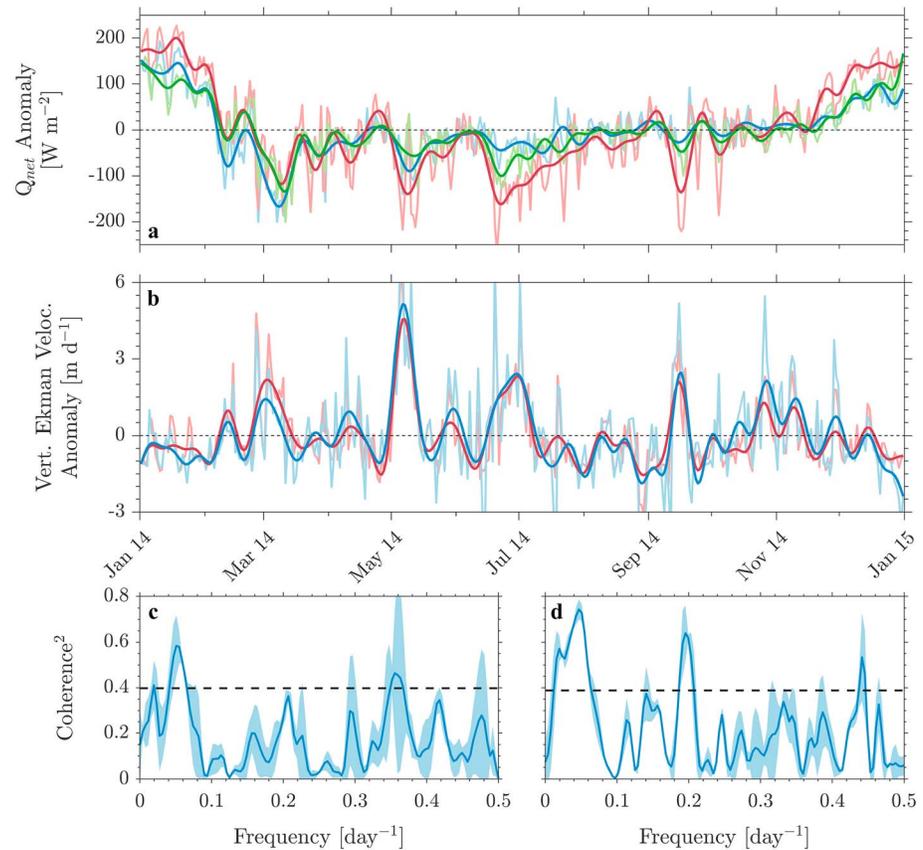
Figure 6. Atmosphere-ocean conditions over Pine Island Bay. (a) Time series of 2014 surface heat flux anomalies averaged over Pine Island Bay derived from ERA5 (blue), CFSR (red), and Tamura (green). (b) Time series of 2014 vertical Ekman velocity anomalies average over PIB derived from ERA5 (blue) and CFSR (red). The thick lines in (a) and (b) have been smoothed with a 10- to 15-day low-pass Kaiser-Bessel filter in order to isolate monthly and longer timescale variability. (c) Average magnitude-squared coherence between the daily averaged surface heat flux anomalies derived from ERA5, CFSR, and Tamura, and the daily averaged melt rate time series. (d) Average magnitude-squared coherence between the daily averaged vertical Ekman velocity anomalies derived from ERA5 and CFSR, and the daily averaged melt rate time series. The light blue envelope in (c) and (d) indicates ±1 standard deviation, and the black dashed line marks the 95% confidence level.

The sign of the correlation, however, is negative. Therefore, while surface heat flux anomalies are coherent with the basal melt rate, they cannot be responsible for driving the observed variability. When the heat content is higher (shallower thermocline; Figure 3b) and melt rate is elevated (e.g., early May or late June 2014; Figure 3a), the surface heat flux anomalies are negative (Figure 6a). Negative anomalies indicate greater heat loss from the ocean, which during these autumn and winter months should act to deepen the thermocline through sea ice formation and convective heat loss. The result should be a reduction in melt rate, contrary to what is observed. Similarly, when heat input to the surface ocean is greater (e.g., late February or mid-March 2014; Figure 6a), we see reduced, rather than elevated, basal melting (Figure 3a). Therefore, while surface heat flux anomalies undoubtedly affect surface ocean conditions in PIB, our observations suggest that they do not propagate far enough into the water column on the timescales considered here to affect basal melting at the location of the ApRES. Indeed, if surface heat fluxes were the major driver, we might expect to see an imprint of their annual cycle on the basal melt rate, as the annual cycle is substantially larger in magnitude than the individual peaks and troughs in the surface heat flux anomaly time series (Figure 6a).

In contrast, positive correlation is observed between the basal melt rate and the vertical Ekman velocity anomalies derived from ERA5 and CFSR and averaged over PIB (Figure 6b). Although the mean vertical Ekman velocity is positive (1.4 m/day and 1.2 m/day for ERA5 and CFSR, respectively), and likely important for the formation of the cyclonic gyre found in front of PIIS (Heywood et al., 2016; Naveira Garabato et al., 2017; Thurnherr et al., 2014), when the vertical Ekman velocity is anomalously strong (e.g., early May 2014),
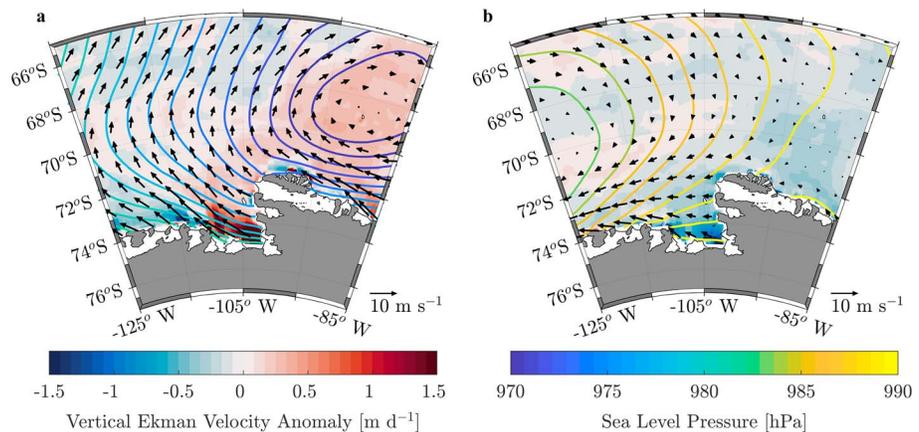
Figure 7. Composite vertical Ekman velocity, surface pressure, and wind vector maps. Mean spatial pattern of the vertical Ekman velocity anomaly (filled contours), 10-m wind vectors (black arrows), and sea level pressure (colored contour lines) derived from ERA5 during (a) peaks (>5 m/year) and (b) troughs (<2 m/year) in the 2014 basal melt rate time series.

the basal melt rate is elevated. When vertical Ekman velocity is anomalously weak (e.g., September 2014), the basal melt rate is reduced. The average magnitude-squared coherence between the vertical Ekman velocity and the basal melt rate (Figure 6d) shows strong peaks at both the monthly (0.05 day^{-1}) and synoptic/weekly (0.2 day^{-1}) frequencies.

The average phase lag derived from the cross spectrum (not shown) that is associated with the peak in coherence at monthly timescales is 23.6°, indicating that the basal melt rate lags changes in the vertical Ekman velocity by 1.4 days. Similarly, the average phase lag at synoptic timescales is 89.9°, corresponding to a comparable time lag of 1.3 days. This suggests that a strong dynamic coupling exists between local wind-driven changes in the thermocline depth over PIB and basal melting at the location of the ApRES. Simple geostrophic adjustment theory would suggest that the 50-km wide gyre in PIB (Heywood et al., 2016; Thurnherr et al., 2014) should adjust to a change in the vertical Ekman velocity on the timescale of 2 to 3 days, while a thermocline anomaly associated with a baroclinic Kelvin wave would take approximately 1 day to propagate from PIB into the sub-ice shelf cavity (see Appendix A for more details). Both of these processes are consistent with the phase lag estimates presented above.

We therefore propose that dynamic adjustment of the thermocline to local wind forcing over PIB was the dominant, short-timescale control on observed basal melt rate throughout 2014. During periods of high basal melting, strong southeasterly winds associated with deeper and more easterly positioned synoptic-scale cyclones at the shelf break drive stronger local Ekman upwelling through an elevated wind-stress curl (Figure 7a). The elevated vertical Ekman velocity shoals the thermocline and creates a warm anomaly that is rapidly propagated into the sub-ice shelf cavity within approximately 2 days. The warm anomaly increases the heat content/thermal driving at the base of the ice shelf, generating a peak in the basal melt rate (thermal driving is the difference between the in situ temperature and freezing point). In contrast, weaker cyclones at the shelf break drive periods of low basal melting. The reduction in local Ekman upwelling leads to a deepening of the thermocline and the formation of a cold anomaly that propagates into the cavity and lowers the heat content/thermal driving at the base of the ice shelf (Figure 7b). Overall, the magnitude-squared coherence indicates that variability in the vertical Ekman velocity can explain 74% of the variance in the observed melt rate at monthly timescales, and 64% at synoptic timescales. The remaining fraction of variance in the basal melt rate that cannot be attributed to variability in the vertical Ekman velocity is likely associated with secondary processes not discussed here, such as coastal upwelling and downwelling.

While there is strong coherence between the vertical Ekman velocity and the basal melt rate at weekly frequencies (Figure 6d), the relative size of the peak at these frequencies in the variance preserving form of the power spectra is much larger for the basal melt rate (Figure 4) than for the vertical Ekman velocity (not shown). This suggests that the basal melt rate responds preferentially to variability in the wind forcing at weekly frequencies, and this preferential response is likely related to the complex adjustment processes through which variability in the vertical Ekman velocity sets the basal melt rate.
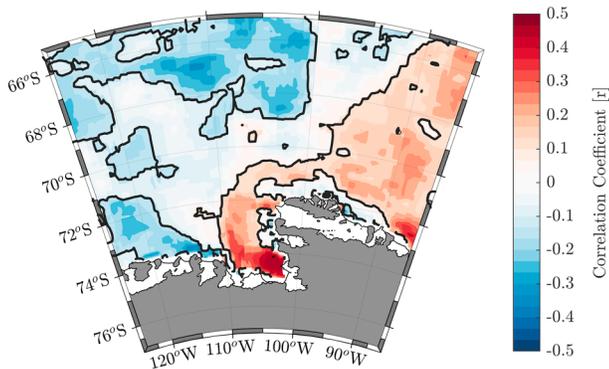
Figure 8. Vertical Ekman velocity spatial correlation. Spatial correlation between the 10 to 15-day low-pass Kaiser-Bessel filtered melt rate time series at the location of the autonomous phase-sensitive radio-echo sounder, and the similarly filtered vertical Ekman velocity time series derived from ERA5 at each point in the Amundsen Sea. The black contours outline regions that are statistically significant at the 95% confidence level.

The local nature of the forcing is reinforced by examining the 2014 spatial correlation between the 10- to 15-day low-pass filtered melt rate time series (Figure 3a), and the similarly filtered time series of vertical Ekman velocity anomalies derived from ERA5 at every point in the Amundsen Sea (Figure 8). The correlation is strongest near PIIS ($r = 0.5$) and decreases with distance from the ice shelf front. The tongue of positive correlation that extends eastward from the Amundsen Sea is due to autocorrelation within the vertical Ekman velocity field. The negative correlation north of the Amundsen Sea arises from the tendency of the vertical Ekman velocity in this region to have a sign opposite to that in front of PIIS.

The occurrence of strong winds during periods of elevated basal melting (Figure 7a) explains the coherence (but negative correlation) that is observed between the basal melt rate and atmosphere-ice-ocean surface heat fluxes. Strong winds (especially those during winter) increase heat loss from the surface ocean through elevated latent and sensible heat fluxes (negative Q_{net} in Figure 6a) and should lead to conditions favorable for reduced basal melting (vice versa for weak winds). However, the heat loss cannot penetrate deep enough to affect the basal melt rate on the short timescales of interest here, and its effect is offset by the Ekman-induced shoaling of the thermocline that drives elevated basal melting.
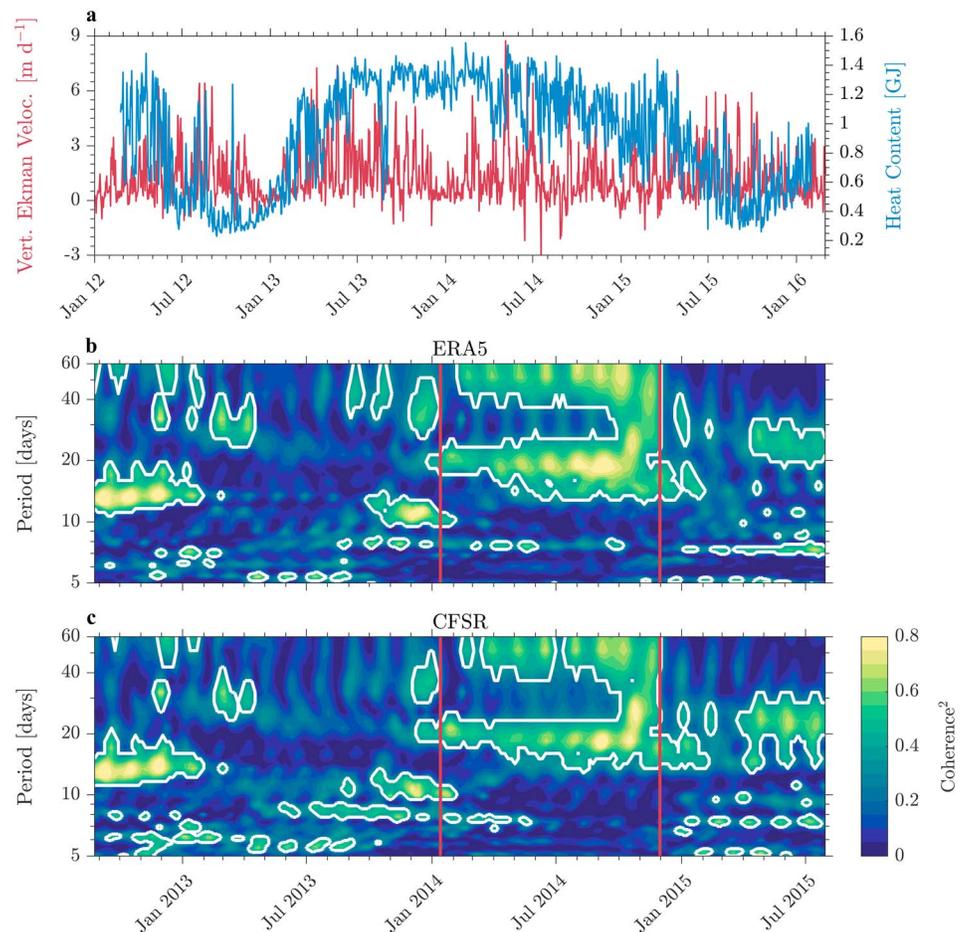
3.3. Long-Term Context

As direct observations of basal melt rate are not available beyond 2014, it is not clear what role local wind forcing may play in other years. It is well known that processes such as shelf edge winds (Wåhlin et al., 2013), equatorial Pacific teleconnections (Steig et al., 2012), atmosphere-ocean heat fluxes, sea ice formation, and changes in local ocean circulation (Webber et al., 2017) are all important in determining the depth of the mCDW thermocline on annual to interannual timescales, and this may have a significant impact on the high-frequency coupling between local winds, thermocline depth, and basal melt rate beneath the outer PIIS.

To explore the longer-term context, we utilize data from the oceanographic moorings in PIB that date back to 2009. In particular, we examine the 2012 to 2016 coherence between the vertical Ekman velocity derived from ERA5 and CFSR and the time series of ocean heat content (i.e., thermocline depth) integrated between 375 and 525 m at the southern mooring in PIB (Figure 9a). The analysis is restricted to begin in 2012 as sufficiently shallow observations are not available prior to this date, and the integration range is slightly deeper than that used earlier due to iceberg dragging of the mooring in 2016 (Figure 5b). The 4 year-long time series is split into 214 individual overlapping yearly segments each separated by 5 days, and the coherence is calculated for each segment independently (Figures 9b and 9c).

While strong coherence at monthly timescales is very prominent during 2014, it is less clear during 2012, 2013, and 2015. During these periods PIB underwent intense cooling (Dutrieux, De Rydt, et al., 2014; Webber et al., 2017; Figure 5), and the integrated ocean heat content in PIB is substantially lower (Figure 9a), indicating a deeper thermocline. Thus, it appears that 2014 may have been a somewhat anomalous year, with local wind forcing setting the variability in the basal melt rate at short timescales. During other years, a wider, long-term deepening of the thermocline in PIB driven by longer timescale processes may have reduced the sensitivity of its depth to local wind forcing, suppressing the high-frequency coupling between winds and basal melt rate beneath the outer PIIS. This highlights the complex interplay that exists between the processes that set the basal melt rate on different timescales. Extending the observational time series of basal melt rate is critical to improve our understanding of the long-term interaction between these processes.

4. Discussion

From the available data, we are confident that during 2014 a strong dynamic coupling existed between changes in local wind forcing over PIB and variability in the basal melt rate beneath the outer PIIS. We acknowledge, however, that the exact mechanism by which variability in the vertical Ekman velocity sets the basal melt rate is not well understood. Here we have adopted the simplest possible explanation:

Figure 9. Long-term coherence between the vertical Ekman velocity and integrated ocean heat content. (a) Long-term time series of vertical Ekman velocity derived from ERA5 (red) and ocean heat content integrated between 375 and 525 m at the southern oceanographic mooring in Pine Island Bay (blue). (b, c) Coherence as a function of time between the ocean heat content at the southern mooring integrated between 375 and 525 m (blue line in panel a) and the vertical Ekman velocity derived from (b) ERA5 (red line in panel a) and (c) CFSR (time series not shown in panel a for clarity). White contours indicate where the coherence is statistically significant at the 95% confidence level, and the red lines indicate the period of time the melt rate was observed directly with the ApRES. The coherence at each point in time represents the coherence derived from a 1-year time series of ocean heat content and vertical Ekman velocity centered on that date.

variability in the vertical Ekman velocity sets the depth of the thermocline and thus the heat content/thermal driving at the base of the ice shelf. Given the importance of understanding the atmosphere-ocean-ice interactions that are responsible for driving the widespread thinning of Antarctic ice shelves, a more detailed study of the pertinent processes and their timescales is warranted. Such a study will necessitate the development of a long-term oceanographic monitoring program beneath PIIS, or a high-resolution ice shelf-ocean model that accurately resolves the important exchange processes that occur at the ice front.

Nevertheless, by multiplying the time-integrated vertical Ekman velocity by the mean temperature gradient over the mCDW thermocline, we can provide an upper-bound estimate on the change in basal melt rate that can be driven by variability in thermocline depth. For example, between 25 April and 6 May 2014, the vertical Ekman velocity caused the thermocline to deepen by about 15 to 25 m over PIB, depending on the reanalysis product (Figure 6b). With a mean thermocline temperature gradient of $5.4 \pm 2.6 \times 10^{-3}$ °C/m at the southern mooring, this corresponds to a temperature anomaly of 0.11 ± 0.06 °C. Using the canonical three-equation melt rate model (Jenkins, Nicholls, et al., 2010) with parameters suitable for beneath PIIS (Stanton et al., 2013; see Appendix B), an upper bound estimate of the change in melt rate due to this temperature anomaly

is 4.1 ± 2.7 m/year. This is on the order of the observed increased in melt rate over the same period (6 to 7 m/year), confirming that changes in thermocline depth are sufficient to drive the observed variability in basal melting.

Basal melting beneath PIIS is highly variable in space (Dutrieux et al., 2013; Dutrieux, Stewart, et al., 2014; Shean et al., 2017), with basal channels modulating the large-scale mean melt rate by 40%–50%. As the ApRES was located on the flank of a channel (Figures 1b and 1c), it is possible that the observed variability in the basal melt rate is not representative of the variability over a wider geographical area. However, given the nature of the local wind forcing and its strong geographic coherency over PIB and parts of the wider Amundsen Sea embayment, there is reason to believe that the short-term temporal variability is coherent over the outer PIIS. Nevertheless, further observations of basal melt rate will be required to confirm whether this is the case. Any geographic coherency, however, is unlikely to extend all the way to the grounding line, as the increasing depth of the ice shelf base will eventually insulate the melt rate from the effects of the short-term variability discussed here. Instead, variability in this region is likely to be more subdued and geographically patchy as the deep inflow of mCDW interacts with the topographically controlled buoyant plumes of meltwater that rise up the steeply sloping ice shelf base (Jenkins, 1991). While thinning near the grounding line is critically important for the stability and evolution of Pine Island Glacier and its ice shelf (De Rydt et al., 2014; Favier et al., 2014), it is not clear whether high-frequency variability in the basal melt rate beneath the outer PIIS can have a similar effect. Modeling studies that include both the long-term processes and the short-timescale forcing discussed here will help us address these questions in the future.

5. Conclusion

Here we have presented a point time series of basal melt rate at sub-weekly resolution from beneath the outer PIIS during 2014 and have explored the dynamic coupling between the melt rate and atmosphere-ocean conditions on weekly to monthly timescales. We propose that adjustment of the thermocline to local variability in the vertical Ekman velocity over PIB is the dominant control on basal melting. Deeper and more easterly positioned synoptic scale cyclones at the shelf break drive stronger Ekman upwelling, a shallower thermocline, and elevated basal melting. In contrast, weaker cyclones result in reduced Ekman upwelling, a deeper thermocline, and lower basal melting. The variability in the vertical Ekman velocity offsets the effect of atmosphere-ice-ocean surface heat fluxes. During other years (2012, 2013, and 2015), annual to interannual variability in the depth of the thermocline in PIB reduces the sensitivity of the melt rate beneath the outer PIIS to local wind forcing, removing the high-frequency coupling observed here. These years are anomalous themselves, however, exhibiting substantially colder conditions in PIB than during any of the preceding three years (2009 to 2011; Figure 5). During these warmer years the thermocline was shallower, and we might expect to have seen a greater sensitivity of the melt rate to local wind forcing. If the thermocline was too shallow, however, local wind-forced variability in thermocline height may not have been able to propagate under the ice shelf, reducing the sensitivity of the melt rate to its variability. Therefore, 2014 may have been a year characterized by a thermocline height that was perfectly positioned for the short (weekly to monthly) timescale variability discussed here to impact the melt rate beneath the outer PIIS. This highlights the complexity of the processes and the timescales involved in the ice-ocean-atmosphere system that ultimately sets the basal melt rate beneath PIIS. It is therefore important to continue exploring the dynamics of this system, so that we can understand fully the role that PIG and other major outlet glaciers found in the Amundsen Sea (e.g., Thwaites) and around the wider Antarctic continent will continue to play in sea level rise over the coming decades.

Appendix A: Adjustment Timescales

A1. Kelvin Wave Phase Speed

The phase speed of a baroclinic Kelvin wave is given by

$$c = \sqrt{g'h},$$

where g' is the reduced gravity and h is a representative depth scale. In PIB, where the reduced gravity is 0.002 m/s² and the depth of the thermocline is 700 m (Thurnherr et al., 2014), a Kelvin wave will have a

phase speed of approximately 1.14 m/s. Assuming a representative horizontal scale of 100 km, a thermocline anomaly associated with a Kelvin wave will therefore take approximately 1 day to propagate from PIB into the sub-ice shelf cavity.

A2. Geostrophic Adjustment Timescale

The geostrophic adjustment problem describes the process by which a fluid adjusts from an initial unbalanced disturbance toward a final quasi-steady geostrophic state (Rossby, 1938). In the context of this study this would be the adjustment of the gyre found in PIB to a perturbation in the density field driven by a change in the vertical Ekman velocity. The timescale for adjustment within a distance on the order of the Rossby radius from the disturbance is given by the inertial period:

$$\frac{2\pi}{f}$$

where f is the Coriolis parameter. In PIB where the baroclinic Rossby radius

$$a = c \left| f^{-1} \right|$$

(c is the baroclinic Kelvin wave speed) is 8.2 km and the inertial period is 12 hr, the adjustment timescale for the gyre in PIB that has a representative horizontal scale of 50 km would be 3 days.

Appendix B: Three-Equation Melt Rate Model

The three-equation melt rate model parameterizes basal melting at the ice-shelf ocean interface as a function of thermal driving (the different between the in situ temperature and the in situ freezing point in the mixed layer beneath the ice shelf base) and current velocity (Jenkins, Nicholls, et al., 2010). While these observations are not available from the location of the ApRES, we take representative values of 1.4 °C and 0.13 m/s observed 2.3 m beneath the base of Pine Island Ice Shelf at a location with a similar ice draft (Stanton et al., 2013). The melt rate also depends on the nondimensional Thermal Stanton number, which we vary between 4.5×10^{-4} and 1.3×10^{-3} due to the unknown drag coefficient at the ice shelf-ocean interface.

References

Arndt, J. E., Schenke, H. W., Jakobsson, M., Nitsche, F. O., Buys, G., Goleby, B., et al. (2013). The International Bathymetric Chart of the Southern Ocean (IBCSO) version 1.0—A new bathymetric compilation covering circum-Antarctic waters. *Geophysical Research Letters*, *40*, 3111–3117. https://doi.org/10.1002/grl.50413

Bamber, J. L., Riva, R. E. M., Vermeersen, B. L. A., & LeBrocq, A. M. (2009). Reassessment of the potential sea-level rise from a collapse of the West Antarctic Ice Sheet. *Science*, *324*(5929), 901–903. https://doi.org/10.1126/science.1169335

Bindschadler, R., Choi, H., Wichlacz, A., Bingham, R., Bohlander, J., Brunt, K., et al. (2011). Getting around Antarctica: New high-resolution mappings of the grounded and freely-floating boundaries of the Antarctic ice sheet created for the International Polar Year. *The Cryosphere*, *5*(3), 569–588. https://doi.org/10.5194/tc-5-569-2011

Christianson, K., Bushuk, M., Dutrieux, P., Parizek, B. R., Joughin, I. R., Alley, R. B., et al. (2016). Sensitivity of Pine Island Glacier to observed ocean forcing. *Geophysical Research Letters*, *43*, 10,817–10,825. https://doi.org/10.1002/2016GL070500

De Rydt, J., Holland, P. R., Dutrieux, P., & Jenkins, A. (2014). Geometric and oceanographic controls on melting beneath Pine Island Glacier. *Journal of Geophysical Research: Oceans*, *119*, 2420–2438. https://doi.org/10.1002/2013JC009513

Deb, P., Orr, A., Bromwich, D. H., Nicolas, J. P., Turner, J., & Hosking, J. S. (2018). Summer drivers of atmospheric variability affecting ice shelf thinning in the Amundsen Sea Embayment, West Antarctica. *Geophysical Research Letters*, *45*, 4124–4133. https://doi.org/10.1029/2018GL077092

DeConto, R. M., & Pollard, D. (2016). Contribution of Antarctica to past and future sea-level rise. *Nature*, *531*(7596), 591–597. https://doi.org/10.1038/nature17145

Dee, D. P., Uppala, S. M., Simmons, A. J., Berrisford, P., Poli, P., Kobayashi, S., et al. (2011). The ERA-interim reanalysis: Configuration and performance of the data assimilation system. *Quarterly Journal of the Royal Meteorological Society*, *137*(656), 553–597. https://doi.org/10.1002/qj.828

Dutrieux, P., De Rydt, J., Jenkins, A., Holland, P. R., Ha, H. K., Lee, S. H., et al. (2014). Strong sensitivity of Pine Island ice-shelf melting to climatic variability. *Science*, *343*(6167), 174–178. https://doi.org/10.1126/science.1244341

Dutrieux, P., Stewart, C., Jenkins, A., Nicholls, K. W., Corr, H. F. J., Rignot, E., & Steffen, K. (2014). Basal terraces on melting ice shelves. *Geophysical Research Letters*, *41*, 5506–5513. https://doi.org/10.1002/2014GL060618

Dutrieux, P., Vaughan, D. G., Corr, H. F. J., Jenkins, A., Holland, P. R., Joughin, I., & Fleming, A. H. (2013). Pine Island glacier ice shelf melt distributed at kilometre scales. *The Cryosphere*, *7*(5), 1543–1555. https://doi.org/10.5194/tc-7-1543-2013

European Centre for Medium-Range Weather Forecasts (ECMWF) (2018a). ERA5 data documentation. Retrieved July 16, 2018, from https://confluence.ecmwf.int//display/CKB/ERA5+data+documentation

ECMWF (2018b). What are the changes from ERA-Interim to ERA5? Retrieved July 16, 2018, from https://confluence.ecmwf.int/pages/viewpage.action?pageId=74764925

Emery, W. J., & Thompson, R. E. (2001). *Data analysis methods in physical oceanography* (2nd ed.). Amsterdam, Netherlands: Elsevier B.V.

Favier, L., Durand, G., Cornford, S. L., Gudmundsson, G. H., Gagliardini, O., Gillet-Chaulet, F., et al. (2014). Retreat of Pine Island Glacier controlled by marine ice-sheet instability. *Nature Climate Change*, *4*(2), 117–121. https://doi.org/10.1038/nclimate2094

Fürst, J. J., Durand, G., Gillet-Chaulet, F., Tavard, L., Rankl, M., Braun, M., & Gagliardini, O. (2016). The safety band of Antarctic ice shelves. *Nature Climate Change*, *6*(5), 479–482. https://doi.org/10.1038/nclimate2912

Greene, C. A., Blankenship, D. D., Gwyther, D. E., Silvano, A., & van Wijk, E. (2017). Wind causes Totten Ice Shelf melt and acceleration. *Science Advances*, *3*(11), e1701681. https://doi.org/10.1126/sciadv.1701681

Heywood, K., Biddle, L., Boehme, L., Dutrieux, P., Fedak, M., Jenkins, A., et al. (2016). Between the devil and the deep Blue Sea: The role of the Amundsen Sea continental shelf in exchanges between ocean and ice shelves. *Oceanography*, *29*(4), 118–129. https://doi.org/10.5670/oceanog.2016.104

IMBIE (2018). Mass balance of the Antarctic Ice Sheet from 1992 to 2017. *Nature*, *558*(7709), 219–222. https://doi.org/10.1038/s41586-018-0179-y

Jacobs, S. S., Jenkins, A., Giulivi, C. F., & Dutrieux, P. (2011). Stronger ocean circulation and increased melting under Pine Island Glacier ice shelf. *Nature Geoscience*, *4*(8), 519–523. https://doi.org/10.1038/ngeo1188

Jenkins, A. (1991). A one-dimensional model of ice shelf-ocean interaction. *Journal of Geophysical Research*, *96*(C11), 20671–20,677. https://doi.org/10.1029/91JC01842

Jenkins, A., Dutrieux, P., Jacobs, S., Steig, E., Gudmundsson, H., Smith, J., & Heywood, K. (2016). Decadal ocean forcing and Antarctic ice sheet response: Lessons from the Amundsen Sea. *Oceanography*, *29*(4), 106–117. https://doi.org/10.5670/oceanog.2016.103

Jenkins, A., Dutrieux, P., Jacobs, S. S., McPhail, S. D., Perrett, J. R., Webb, A. T., & White, D. (2010). Observations beneath Pine Island Glacier in West Antarctica and implications for its retreat. *Nature Geoscience*, *3*(7), 468–472. https://doi.org/10.1038/ngeo890

Jenkins, A., Nicholls, K. W., & Corr, H. F. J. (2010). Observation and parameterization of ablation at the base of Ronne Ice Shelf, Antarctica. *Journal of Physical Oceanography*, *40*(10), 2298–2312. https://doi.org/10.1175/2010JPO4317.1

Jones, R. W., Renfrew, I. A., Orr, A., Webber, B. G. M., Holland, D. M., & Lazzara, M. A. (2016). Evaluation of four global reanalysis products using in situ observations in the Amundsen Sea Embayment, Antarctica. *Journal of Geophysical Research: Atmospheres*, *121*, 6240–6257. https://doi.org/10.1002/2015JD024680

Khazendar, A., Schodlok, M. P., Fenty, I., Ligtenberg, S. R. M., Rignot, E., & van den Broeke, M. R. (2013). Observed thinning of Totten Glacier is linked to coastal polynya variability. *Nature Communications*, *4*(1), 2857. https://doi.org/10.1038/ncomms3857

Kim, T. W., Ha, H. K., Wåhlin, A. K., Lee, S. H., Kim, C. S., Lee, J. H., & Cho, Y. K. (2017). Is Ekman pumping responsible for the seasonal variation of warm circumpolar deep water in the Amundsen Sea? *Continental Shelf Research*, *132*, 38–48. https://doi.org/10.1016/j.csr.2016.09.005

Kimura, S., Jenkins, A., Regan, H., Holland, P. R., Assmann, K. M., Whitt, D. B., et al. (2017). Oceanographic controls on the variability of ice-shelf basal melting and circulation of glacial meltwater in the Amundsen Sea Embayment, Antarctica. *Journal of Geophysical Research: Oceans*, *122*, 10,131–10,155. https://doi.org/10.1002/2017JC012926

Lok, L. B., Nicholls, K., Brennan, P. V., & Davis, P. (2018). *Basal melt rate beneath pine island ice shelf (2014)*. Polar Data Centre, Natural Environment Research Council, UK Research & Innovation. https://doi.org/10.5285/0cf552a6-cd62-4da0-8289-8e4bab0a35a8

Mallett, H. K. W., Boehme, L., Fedak, M., Heywood, K. J., Stevens, D. P., & Roquet, F. (2018). Variation in the distribution and properties of Circumpolar Deep Water in the eastern Amundsen Sea, on seasonal timescales, using seal-borne tags. *Geophysical Research Letters*, *45*, 4982–4990. https://doi.org/10.1029/2018GL077430

McDougall, T. J., & Barker, P. M. (2011). Getting started with TEOS-10 and the Gibbs Seawater (GSW) Oceanographic Toolbox. SCOR/IAPSO WG127.

McMillan, M., Shepherd, A., Sundal, A., Briggs, K., Muir, A., Ridout, A., et al. (2014). Increased ice losses from Antarctica detected by CryoSat-2. *Geophysical Research Letters*, *41*, 3899–3905. https://doi.org/10.1002/2014GL060111

Millan, R., Rignot, E., Bernier, V., Morlighem, M., & Dutrieux, P. (2017). Bathymetry of the Amundsen Sea Embayment sector of West Antarctica from Operation IceBridge gravity and other data. *Geophysical Research Letters*, *44*, 1360–1368. https://doi.org/10.1002/2016GL072071

Mouginot, J., Rignot, E., & Scheuchl, B. (2014). Sustained increase in ice discharge from the Amundsen Sea Embayment, West Antarctica, from 1973 to 2013. *Geophysical Research Letters*, *41*, 1576–1584. https://doi.org/10.1002/2013GL059069

Naveira Garabato, A. C., Forryan, A., Dutrieux, P., Brannigan, L., Biddle, L. C., Heywood, K. J., et al. (2017). Vigorous lateral export of the meltwater outflow from beneath an Antarctic ice shelf. *Nature*, *542*(7640), 219–222. https://doi.org/10.1038/nature20825

Nicholls, K. W., Corr, H. F. J., Stewart, C. L., Lok, L. B., Brennan, P. V., & Vaughan, D. G. (2015). A ground-based radar for measuring vertical strain rates and time-varying basal melt rates in ice sheets and shelves. *Journal of Glaciology*, *61*(230), 1079–1087. https://doi.org/10.3189/2015JoG15J073

Padman, L., Costa, D. P., Dinniman, M. S., Fricker, H. A., Goebel, M. E., Huckstadt, L. A., et al. (2012). Oceanic controls on the mass balance of Wilkins Ice Shelf, Antarctica. *Journal of Geophysical Research*, *117*, C01010. https://doi.org/10.1029/2011JC007301

Paolo, F. S., Fricker, H. A., & Padman, L. (2015). Volume loss from Antarctic ice shelves is accelerating. *Science*, *348*(6232), 327–331. https://doi.org/10.1126/science.aaa0940

Pritchard, H. D., Ligtenberg, S. R. M., Fricker, H. A., Vaughan, D. G., van den Broeke, M. R., & Padman, L. (2012). Antarctic ice-sheet loss driven by basal melting of ice shelves. *Nature*, *484*(7395), 502–505. https://doi.org/10.1038/nature10968

Rignot, E., Mouginot, J., Morlighem, M., Seroussi, H., & Scheuchl, B. (2014). Widespread, rapid grounding line retreat of Pine Island, Thwaites, smith, and Kohler glaciers, West Antarctica, from 1992 to 2011. *Geophysical Research Letters*, *41*, 3502–3509. https://doi.org/10.1002/2014GL060140

Rossby, C.-G. (1938). On the mutual adjustment of pressure and velocity distributions in certain simple current systems, II. *Journal of Marine Research*, *1*(3), 239–263. https://doi.org/10.1357/002224038806440520

Saha, S., Moorthi, S., Pan, H.-L., Wu, X., Wang, J., Nadiga, S., et al. (2010). The NCEP climate forecast system reanalysis. *Bulletin of the American Meteorological Society*, *91*(8), 1015–1058. https://doi.org/10.1175/2010BAMS3001.1

Scheuchl, B., Mouginot, J., Rignot, E., Morlighem, M., & Khazendar, A. (2016). Grounding line retreat of Pope, Smith, and Kohler Glaciers, West Antarctica, measured with Sentinel-1a radar interferometry data. *Geophysical Research Letters*, *43*, 8572–8579. https://doi.org/10.1002/2016GL069287

Shean, D. E. (2016). Quantifying ice-shelf basal melt and ice-stream dynamics using high-resolution DEM and GPS time series. (PhD Thesis). Seattle, WA: University of Washington.

Shean, D. E., Alexandrov, O., Moratto, Z. M., Smith, B. E., Joughin, I. R., Porter, C., & Morin, P. (2016). An automated, open-source pipeline for mass production of digital elevation models (DEMs) from very-high-resolution commercial stereo satellite imagery. *ISPRS Journal of Photogrammetry and Remote Sensing*, *116*, 101–117. https://doi.org/10.1016/j.isprsjprs.2016.03.012

Shean, D. E., Christianson, K., Larson, K. M., Ligtenberg, S. R. M., Joughin, I. R., Smith, B. E., et al. (2017). GPS-derived estimates of surface mass balance and ocean-induced basal melt for Pine Island Glacier ice shelf, Antarctica. *The Cryosphere*, *11*(6), 2655–2674. https://doi.org/10.5194/tc-11-2655-2017

Shepherd, A., Fricker, H. A., & Farrell, S. L. (2018). Trends and connections across the Antarctic cryosphere. *Nature*, *558*(7709), 223–232. https://doi.org/10.1038/s41586-018-0171-6

Shepherd, A., Ivins, E. R., Gerou, A., Barletta, V. R., Bentley, M. J., Bettadpur, S., et al. (2012). A reconciled estimate of ice-sheet mass balance. *Science*, *338*(6111), 1183–1189. https://doi.org/10.1126/science.1228102

Spreen, G., Kaleschke, L., & Heygster, G. (2008). Sea ice remote sensing using AMSR-E 89-GHz channels. *Journal of Geophysical Research*, *113*, C02S03. https://doi.org/10.1029/2005JC003384

Stanton, T. P., Shaw, W. J., Truffer, M., Corr, H. F. J., Peters, L. E., Riverman, K. L., et al. (2013). Channelized ice melting in the ocean boundary layer beneath Pine Island Glacier, Antarctica. *Science*, *341*(6151), 1236–1239. https://doi.org/10.1126/science.1239373

Steig, E. J., Ding, Q., Battisti, D. S., & Jenkins, A. (2012). Tropical forcing of Circumpolar Deep Water Inflow and outlet glacier thinning in the Amundsen Sea Embayment, West Antarctica. *Annals of Glaciology*, *53*(60), 19–28. https://doi.org/10.3189/2012AoG60A110

Tamura, T., Ohshima, K. I., & Nihashi, S. (2008). Mapping of sea ice production for Antarctic coastal polynyas. *Geophysical Research Letters*, *35*, L07606. https://doi.org/10.1029/2007GL032903

Tamura, T., Ohshima, K. I., Nihashi, S., & Hasumi, H. (2011). Estimation of surface heat/salt fluxes associated with sea ice growth/melt in the Southern Ocean. *SOLA*, *7*, 17–20. https://doi.org/10.2151/sola.2011-005

Thoma, M., Jenkins, A., Holland, D., & Jacobs, S. (2008). Modelling Circumpolar Deep Water intrusions on the Amundsen Sea continental shelf, Antarctica. *Geophysical Research Letters*, *35*, L18602. https://doi.org/10.1029/2008GL034939

Thurnherr, A. M., Jacobs, S. S., Dutrieux, P., & Giulivi, C. F. (2014). Export and circulation of ice cavity water in Pine Island Bay, West Antarctica. *Journal of Geophysical Research: Oceans*, *119*, 1754–1764. https://doi.org/10.1002/2013JC009307

Tschudi, M., Fowler, C., Maslanik, J., Stewart, J. S., & Meier, W. (2016). Polar Pathfinder daily 25 km EASE-grid sea ice motion vectors, Version 3. Boulder, CO. https://doi.org/10.5067/O57VAIT2AYYY

Wåhlin, A. K., Kalén, O., Arneborg, L., Björk, G., Carvajal, G. K., Ha, H. K., et al. (2013). Variability of warm deep water inflow in a submarine trough on the Amundsen Sea shelf. *Journal of Physical Oceanography*, *43*(10), 2054–2070. https://doi.org/10.1175/JPO-D-12-0157.1

Wåhlin, A. K., Yuan, X., Björk, G., & Nohr, C. (2010). Inflow of warm circumpolar deep water in the Central Amundsen shelf. *Journal of Physical Oceanography*, *40*(6), 1427–1434. https://doi.org/10.1175/2010JPO4431.1

Walker, D. P., Jenkins, A., Assmann, K. M., Shoosmith, D. R., & Brandon, M. A. (2013). Oceanographic observations at the shelf break of the Amundsen Sea, Antarctica. *Journal of Geophysical Research: Oceans*, *118*, 2906–2918. https://doi.org/10.1002/jgrc.20212

Webber, B. G. M., Heywood, K. J., Stevens, D. P., Dutrieux, P., Abrahamsen, E. P., Jenkins, A., et al. (2017). Mechanisms driving variability in the ocean forcing of Pine Island glacier. *Nature Communications*, *8*, 14507. https://doi.org/10.1038/ncomms14507

Wingham, D. J., Wallis, D. W., & Shepherd, A. (2009). Spatial and temporal evolution of Pine Island glacier thinning, 1995–2006. *Geophysical Research Letters*, *41*, L17501. https://doi.org/10.1002/2014GL060111